Weierstraß–Institut
für Angewandte Analysis und Stochastik

im Forschungsverbund Berlin e.V.

Preprint ISSN 0946 – 8633

Transient numerical investigation of induction heating during sublimation growth of silicon carbide single crystals

Olaf Klein, Peter Philip

submitted: June 6th 2001

Weierstrass Institute
for Applied Analysis
and Stochastics
Mohrenstraße 39
D – 10117 Berlin
Germany
E-Mail: klein@wias-berlin.de
E-Mail: philip@wias-berlin.de

Preprint No. 659
Berlin 2001

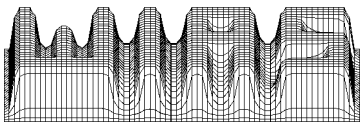

2000 *Mathematics Subject Classification.* 80A20, 65M99, 65Z05, 35K55, 78A55, 78M25.

Key words and phrases. Numerical simulation, sublimation growth, physical vapor transport, modified Lely method, SiC single crystal, induction heating, heat transfer.

1998 PACS numbers. 02.60.Cb, 81.10.Bk, 84.32.Hh, 44.30.+v, 44.90.+c.

Edited by
Weierstraß–Institut für Angewandte Analysis und Stochastik (WIAS)
Mohrenstraße 39
D — 10117 Berlin
Germany

Fax: + 49 30 2044975
E-Mail (X.400): c=de;a=d400-gw;p=WIAS-BERLIN;s=preprint
E-Mail (Internet): preprint@wias-berlin.de
World Wide Web: http://www.wias-berlin.de/

Abstract

This article presents transient numerical simulations of the temperature evolution during sublimation growth of SiC single crystals via physical vapor transport (also called the modified Lely method) including diffusion and radiation, investigating the influence of induction heating. Using the imposed voltage as input data, the heat sources are computed via an axisymmetric complex-valued magnetic scalar potential that is determined as the solution of an elliptic PDE. The presented results include stationary simulations of magnetic potential distributions and resulting heat sources as well as transient simulations of the temperature evolution during the heating process. We examine the effects of imposed voltage (i.e. heating power), of different coil positions, and of a moving induction coil on the evolution of the global temperature field and on the temperature at the source, at the seed, and at the blind holes. All material data used are either included or referenced.

1 Introduction

SiC bulk single crystals provide a semiconductor substrate material used in electronic and optoelectronic devices, e.g. MESFETs, thyristors, LEDs, lasers, and sensors. Due to its physical properties, SiC is especially suitable to be used in high temperature, high power, and high frequency applications as well as in intensive radiation environments.

SiC applications require the availability of large diameter, low defect SiC boules, whose manufacturing process remains challenging inspite of progress made in recent years (cf. e.g. [MGH+00]). We consider the production of SiC single crystals by sublimation growth via *physical vapor transport* (PVT) (modified Lely method, see [Kon95]).

Usually, PVT growth systems consist of an induction-heated graphite crucible containing polycrystalline SiC source powder and a single-crystalline SiC seed cooled by means of a blind hole (cf. Fig. 1). The system is degassed to 10^{-3} Pa and heated to some 1200 K to eliminate contaminants such as nitrogen. At this stage, a high-purity argon (inert gas) atmosphere is established at 10^5 Pa, and the temperature is further increased. At growth temperature, which can reach up to 3000 K for 6H SiC, pressure is reduced to about $2 \cdot 10^3$ Pa (cf. [BMH+93]).

Due to high temperature and low pressure, SiC source powder evaporates, adding species such as Si, Si_2C and SiC_2 to the gas phase. Crystallization occurs at the cooled seed which thereby grows into the reaction chamber.

As the crystal's quality and growth rate depend strongly on the evolution of the temperature distribution (cf. [RSD+99] and [SBP98]), mass transport, and species concentrations (cf. [SVK+00]), control of these quantities is essential. However, due

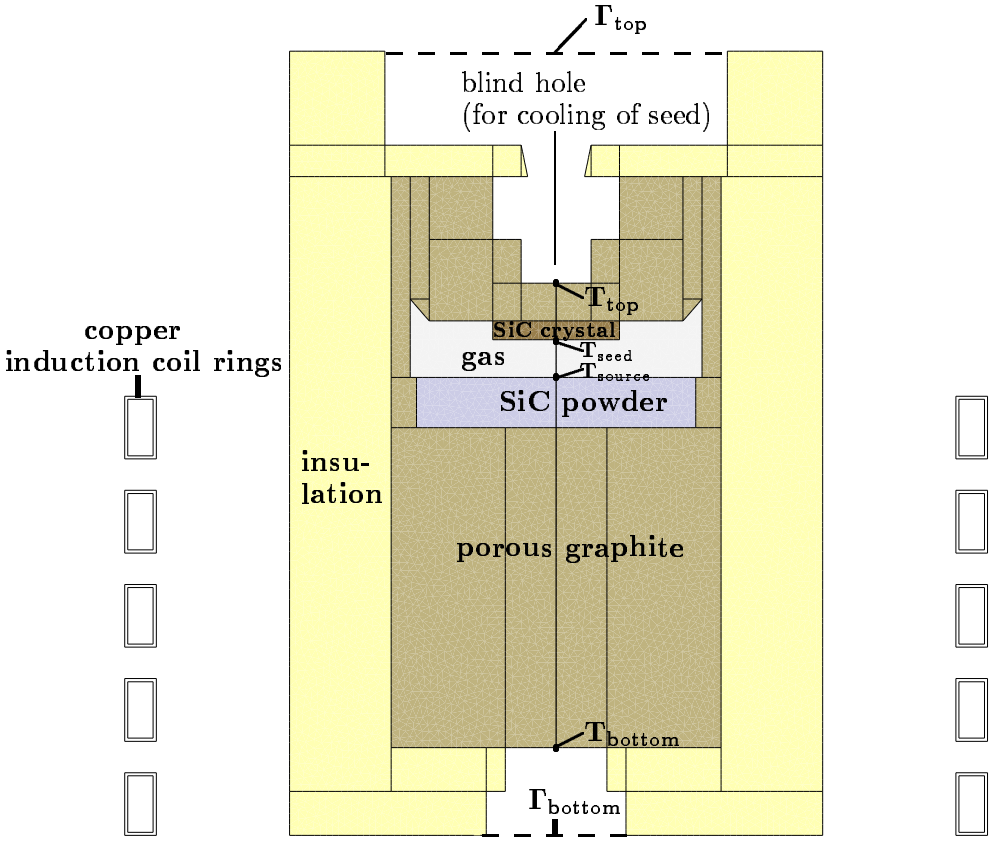

Figure 1: Setup of growth apparatus according to [PAC+99, Fig. 2].

to the high temperatures, experimental verification of the correlation between the quantities to be regulated and control parameters such as apparatus configuration, heating power, and argon pressure is extremely difficult and costly.

Thus, theoretical modeling and numerical simulation play a fundamental role in gaining understanding of the relation between control parameters and favorable growth conditions. Various recent publications report on the development and applications of numerical tools in the framework of PVT, mostly using stationary models (cf. eg. [KMR97], [CAB+99], [PAC+99], [RMD+99], [KKZ+00], and [SKM+00]). Transient numerical results on the evolution of heat transfer during PVT are presented in [CZP+99] and [KPSW01].

Crystal growth can already occur during the heating-up stage, possibly resulting in persisting defects such as micropipes and unwanted polytypes. Moreover, thermal stresses in the seed crystal due to temperature gradients can initiate crystal defects. Therefore one can not restrict ones attention to the quasi-stationary state at the end of the heating process, but it is also important to monitor and control the temperature field evolution during the heating process itself.

The main objective of this work is to numerically investigate induction heating during PVT and to present systematic transient numerical parameter studies of how changes in the heating power and the coil position affect the evolution of the

global temperature field and the evolution of the temperature at significant points such as the seed crystal, the SiC source, and the blind holes at the top and at the bottom of the growth apparatus (cf. Sec. 3.3).

The numerical simulations presented in this paper are performed for the configuration depicted in Fig. 1 taken from [PAC+99, Fig. 2]. We employ the transient heat transport model previously described in detail in [BKP+99] and [KPSW01]. Neglecting any mechanical or chemical interactions inside both solid and gas as well as convective contributions in the gas phase, the heat transport is described by (cf. [KPSW01, (1.4), (1.5), and (3.1)])

$$\rho^{[\beta]} c_{\mathrm{sp}}^{[\beta]} \frac{\partial T}{\partial t} - \operatorname{div}\left(\kappa^{[\beta]} \operatorname{grad} T\right) = \mu^{[\beta]} \qquad \text{(solid component } \beta\text{)}, \tag{1.1a}$$

$$\rho_{\mathrm{gas}} \frac{\partial U_{\mathrm{gas}}}{\partial t} - \operatorname{div}\left(\kappa_{\mathrm{gas}} \operatorname{grad} T\right) = 0 \qquad \text{(gas phase)}, \tag{1.1b}$$

where superscripts $[\beta]$ refer to quantities in the solid component β (β = Insulation, SiC Crystal, ...), and the subscript "gas" refers to quantities in the gas phase. The meaning of the symbols is as follows:

ρ_{gas}, $\rho^{[\beta]}$ – mass density, $c_{\mathrm{sp}}^{[\beta]}$ – specific heat,
T – absolute temperature, t – time,
κ_{gas}, $\kappa^{[\beta]}$ – thermal conductivity, U_{gas} – total internal energy,
$\mu^{[\beta]}$ – power density (per volume) of heat source due to induction heating.

In contrast to [KPSW01], where a homogeneous heat source was assumed inside a prescribed susceptor region, we compute the material- and temperature-dependent heat source distribution according to the position of the induction coil and the voltage imposed therein (cf. Sec. 2).

As in [KPSW01] all temperature simulations assume a gas phase consisting of pure argon. It is explained in [KPSW01, Sec. 5] that this is a reasonable approximation for temperature simulations, notwithstanding the fact that species such as Si, Si_2C and SiC_2 make up a significant portion of the gas mixture for high temperatures. For pure argon the internal energy is

$$U_{\mathrm{gas}} = \frac{3}{2} \frac{R}{M^{(\mathrm{Ar})}} T, \tag{1.2}$$

where R denotes the universal gas constant, and $M^{(\mathrm{Ar})}$ denotes the molecular weight of argon.

Radiative heat transfer between surfaces of cavities is included using the net radiation method for diffuse-gray radiation, where the interface condition between the solid β and the gas phase reads (cf. [KPSW01, (2.1)])

$$\left(\kappa_{\mathrm{gas}} \operatorname{grad} T\right) \bullet \vec{n}_{\mathrm{gas}} + R_{\mathrm{rad}} - J_{\mathrm{rad}} = \left(\kappa^{[\beta]} \operatorname{grad} T\right) \bullet \vec{n}_{\mathrm{gas}}, \tag{1.3}$$

R_{rad} denoting radiosity, J_{rad} denoting irradiation, and $\vec{n}_{\mathrm{gas}}$ denoting the unit normal vector on the interface pointing from gas to solid. All solids are treated as opaque,

except the single crystal, where semi-transparency is accounted for via the band approximation model. Between different solids the heat flux is taken as continuous, except if one solid material is the SiC crystal, in which case semi-transparency causes a discontinuity.

The temperature is presumed to be continuous everywhere in the growth apparatus, disregarding the expected temperature step at gas-solid interfaces, in absence of precise data for transition coefficients.

The Stefan-Boltzmann law provides the outer boundary condition (cf. [KPSW01, (3.3)])

$$-\left(\kappa_{\mathrm{gas}} \operatorname{grad} T\right) \bullet \vec{n}_\beta = \sigma \varepsilon^{[\beta]}(T) \left(T^4 - T_{\mathrm{room}}^4\right), \tag{1.4}$$

σ denoting the Boltzmann radiation constant, ε denoting the emissivity of the surface, and $\vec{n}_\beta$ denoting the outer unit normal vector to the solid material β. Condition (1.4) means that the growth apparatus is exposed to a black body environment (e.g. a large isothermal room) radiating at room temperature T_{room}. Analogously, we use black body phantom closures of open radiation regions such as Γ_{top} and Γ_{bottom} depicted in Fig. 1 which emit radiation at T_{room}, thereby allowing for radiative interactions between an open cavity and the ambient environment including reflections at the cavity's surfaces.

For the numerical simulations of this work, the above equations will be considered in two space dimensions, taking into account the cylindrical symmetry of the growth system.

2 The Induction Heating Model

All solid materials in the growth system are considered potential conductors, whereas the gas phase is treated as a perfect isolator.

The crucible is placed inside a copper induction coil as depicted in Fig. 1. The actual coil is replaced by axisymmetric rings to maintain the cylindrical symmetry of the system. An alternating voltage is imposed in the coil, resulting in an alternating current that generates a rapidly oscillating magnetic field, inducing eddy currents in the growth apparatus. The eddy currents cause heat sources due to the Joule effect. It is assumed that a sinusoidal alternating voltage

$$V(t) = V_0 \sin(\omega t) \tag{2.1}$$

is imposed in the coil, since e.g. in experimental setups at the *Institut für Kristallzüchtung*[1] *(IKZ)* in Berlin the voltage is more easily measured than the current. If the coil consists of N rings, then the voltage in each ring is taken as V/N. The sinusoidal case allows to reduce the time-dependent electromagnetic problem to a stationary one in the presence of constant material parameters. However, to account for the temperature-dependence of the electrical conductivity and for changing coil

[1] Institute of Crystal Growth

positions during the transient simulations in Sec. 3.3, a quasi-stationary electromagnetic problem is solved in each time step of the transient computations.

In cylindrical coordinates (r, z) the power density of the heat sources is given by

$$\mu^{[\beta]}(r,z) = \frac{|j(r,z)|^2}{2\,\sigma_c^{[\beta]}(T(r,z))}, \tag{2.2}$$

where j is the complex-valued current density, and σ_c is the electrical conductivity.

Under the above assumptions, we can use the induction heating model presented in [RS96], where it is shown that there is a complex-valued magnetic scalar potential ϕ such that

$$j = \begin{cases} -i\omega\,\sigma_c^{[\mathrm{Cu}]}\,\phi + \frac{\sigma_c^{[\mathrm{Cu}]}\,V_0}{2\pi r\,N} & \text{in each induction coil ring,} \\ -i\omega\,\sigma_c^{[\beta]}\,\phi & \text{in all other conducting materials } \beta, \end{cases} \tag{2.3}$$

i denoting the imaginary unit (cf. [RS96, Eq. (28)]). The potential ϕ is determined from the system of elliptic partial differential equations [RS96, (22), (29), and (30)] with the boundary condition $\phi = 0$ both on the symmetry axis $r = 0$ and sufficiently far from the growth apparatus (in Sec. 3.2 it is found that using a domain radius and height of 1.2 m and 1.8 m, respectively, is sufficiently accurate for our purposes). We rewrite [RS96, (22), (29), (30)] in terms of the quantity $\psi := r \cdot \phi$, resulting in the following equations which are more suitable for our numerical approach via a finite volume discretization:

$$-\nu_{\mathrm{gas}}\,\mathrm{div}\,\frac{\mathrm{grad}\,\psi}{r^2} = 0 \qquad \text{in the gas phase,} \tag{2.4a}$$

$$-\nu^{[\mathrm{Cu}]}\,\mathrm{div}\,\frac{\mathrm{grad}\,\psi}{r^2} + \frac{i\,\omega\sigma_c^{[\mathrm{Cu}]}\psi}{r^2} = \frac{\sigma_c^{[\mathrm{Cu}]}\,V_0}{2\pi r^2\,N} \qquad \text{in each induction coil ring,} \tag{2.4b}$$

$$-\nu^{[\beta]}\,\mathrm{div}\,\frac{\mathrm{grad}\,\psi}{r^2} + \frac{i\,\omega\sigma_c^{[\beta]}\psi}{r^2} = 0 \qquad \text{in other conducting materials } \beta, \tag{2.4c}$$

$$\left(\frac{\nu_{\mathrm{gas}}}{r^2}\,\mathrm{grad}\,\psi\right) \bullet \vec{n}_{\mathrm{gas}} = \left(\frac{\nu^{[\beta]}}{r^2}\,\mathrm{grad}\,\psi\right) \bullet \vec{n}_{\mathrm{gas}}, \tag{2.5}$$

where ν denotes the reciprocal of the magnetic permeability.

Interface condition (2.5) is valid under the assumption that there are no surface currents. It is also assumed that ϕ (and thus ψ) is continuous throughout the whole domain.

3 Numerical Experiments

3.1 General Setup and Methods

All numerical simulations presented in the following were performed for a growth system consisting of a container with a height of 25 cm and a radius of 8.4 cm

placed inside of 5 hollow rectangular-shaped copper induction rings as displayed in Fig. 1, each ring having a surface thickness of 1 mm. The geometric proportions of the coil rings are depicted in Fig. 2. While the vertical gap between container and coil is fixed at 4.2 cm in all our experiments, the vertical coil position is varied for the simulations in Sec. 3.3. The prescribed heating voltage satisfies (2.1). We fix its frequency at $f = 10$ kHz, whereas we vary the effective voltage such that $190\text{V} \leq V_{\text{eff}} \leq 270\text{V}$. The angular frequency and the amplitude are provided by $\omega = 2\pi f$ and $V_0 = V_{\text{eff}}\sqrt{2}$.

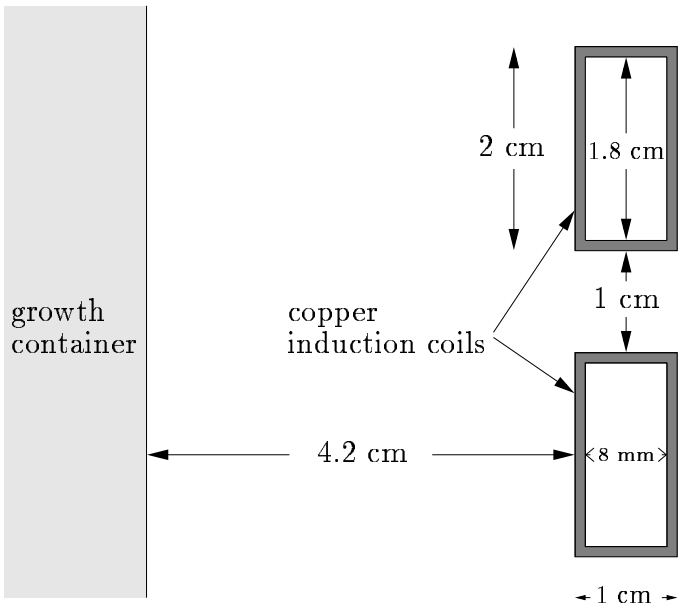

Figure 2: Geometric proportions of induction coil rings.

It is reiterated that only argon is considered in the gas phase and that it is the only material considered a perfect isolator. The solid materials are assumed to be homogeneous and pure materials. In particular inhomogeneities in the source powder, and chemical changes occurring during the growth process such as sintering and graphitization of the source, and Si accumulating in the insulation felt are ignored.

In real growth systems the coil is usually cooled very efficiently, e.g. by water flowing inside the coil rings. Hence it is reasonable to assume that the coil is always at room temperature, its material data not being changed during the experiments.

The complete list of material data used for our numerical simulations of induction heating can be found in App. A. The material parameters used for the simulations of the temperature field evolution are identical to the ones used in [KPSW01] and can be found in [KPSW01, App. A].

A finite volume method based on [Fuh97] is used for the space discretizations arising in the stationary computation of the magnetic scalar potential and in the tran-

sient temperature simulations, where an implicit Euler scheme provides the time discretization. The discrete scheme has been implemented using the *pdelib* program package, being developed at the *Weierstrass Institute of Applied Analysis and Stochastics (WIAS)*, Berlin (cf. [FKL98]). For the numerical methods used for radiation and view factor calculation we refer to [KPSW01, Sec. 4].

3.2 Stationary Computations of Heat Sources

This section presents and discusses results of three stationary computations at $T_{\text{room}} = 293$ K of the magnetic scalar potential ϕ and the resulting power densities μ. In addition, the total heating powers $P_{\text{total}}^{[\text{apparatus}]}$ and $P_{\text{total}}^{[\text{coil}]}$ are computed in the growth apparatus and in the coil rings, respectively, by integrating μ over the corresponding regions. More precisely

$$P_{\text{total}}^{[\text{apparatus}]} = \sum_{\text{solids } \beta \neq \text{ coil rings}} \int_{\text{solid } \beta} \mu^{[\beta]}, \qquad P_{\text{total}}^{[\text{coil}]} = \int_{\text{coil rings}} \mu^{[\text{Cu}]}. \tag{3.1}$$

In practice the integrals in (3.1) are approximated by sums over finite volume elements.

The simulations use $V_{\text{eff}} = 230$ V, the coil's upper rim is at $z = 14$ cm and its lower rim is level with the lower rim of the growth apparatus at $z = 0$. The results show that even though the outcome for the magnetic potential distribution does depend on the size of the domain used in the computation, the arising heat source distribution is not affected significantly. The simulations were performed on domains Ω_{small} (radius $r_{\text{small}} = 0.4$ m, height $h_{\text{small}} = 1.0$ m), Ω_{medium} ($r_{\text{medium}} = 1.2$ m, $h_{\text{medium}} = 1.8$ m), and Ω_{large} ($r_{\text{large}} = 2.8$ m, $h_{\text{large}} = 3.4$ m), the growth apparatus being always approximately in the center of the domain.

It is noted that instead of imposing the boundary condition $\phi = 0$ at $r = 0$, $\phi = 0$ is set at the vertical line $r = 1$ mm, where ϕ is considered to be sufficiently small. This permits the evaluation of terms with r in the denominator (cf. (2.4) and (2.5)).

Figure 3 depicts the results of the three numerical experiments, Ω_{small} in column (a), Ω_{medium} in column (b), and Ω_{large} in column (c). Row (1) shows the imaginary part $\text{Im}(\phi)$ of the magnetic scalar potential with isolevels spaced at $\Delta_{\text{iso}} = 10^{-5}$ Wb/m, row (2) shows the real part $\text{Re}(\phi)$ ($\Delta_{\text{iso}} = 10^{-7}$ Wb/m), and row (3) shows the induced power densities μ ($\Delta_{\text{iso}} = 1$ kW/m^3). The pictures demonstrate that $\text{Im}(\phi)$ reaches rather far into the surrounding space of the growth apparatus, and the calculated global distribution depends noticeably on the size of the domain. The reach of $\text{Re}(\phi)$ is considerably less, as can be seen from the agreement of (2)(b) and (2)(c) in Fig. 3.

However, in a close neighborhood of the growth apparatus and the coil rings the distributions of $\text{Im}(\phi)$ and $\text{Re}(\phi)$ are almost identical for the three domains. This results in virtually identical power density distributions (s. row (3) of Fig. 3). Moreover, the values in Tab. 1 show that the ranges of $\text{Im}(\phi)$, $\text{Re}(\phi)$, and μ (both in

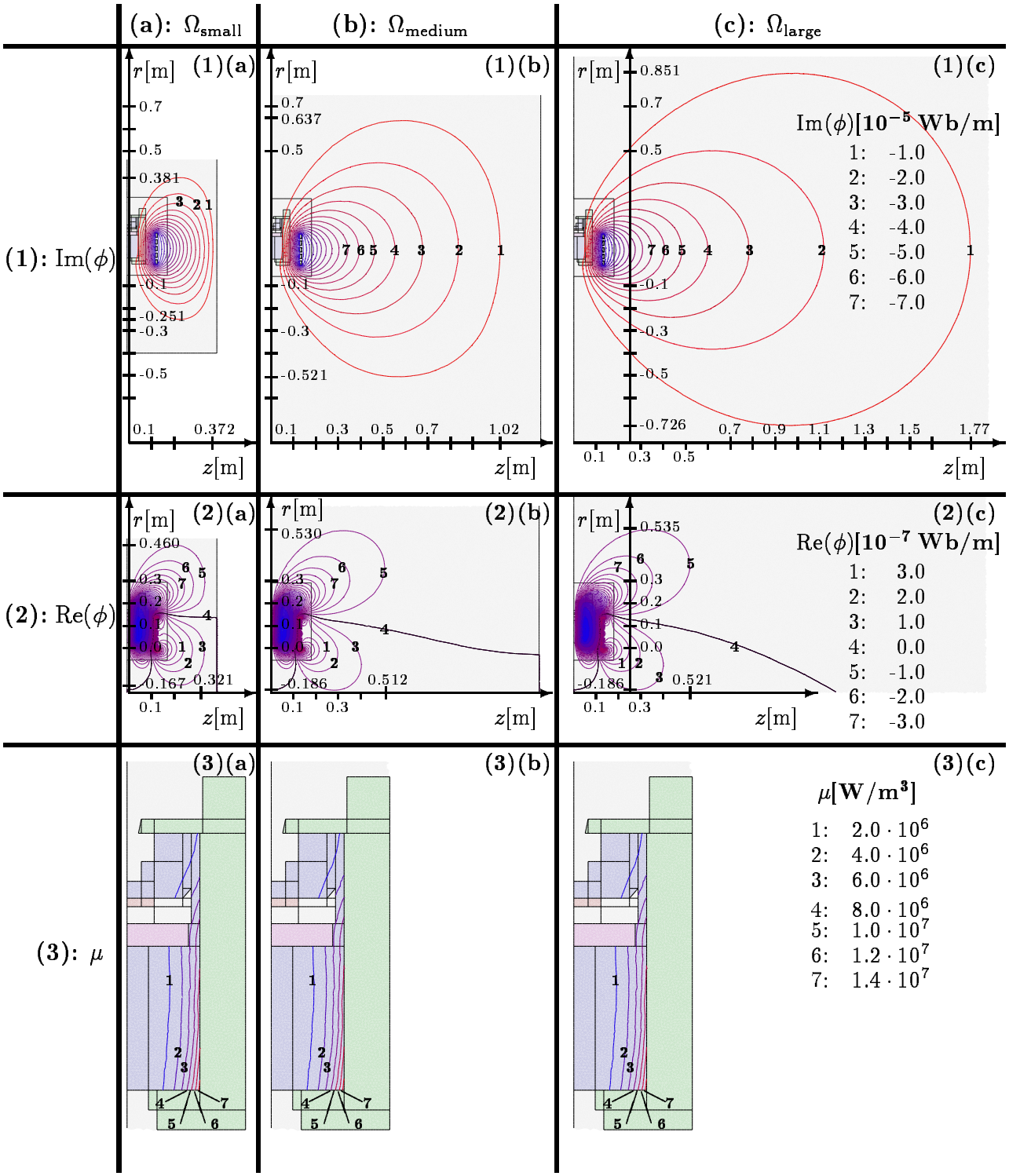

Figure 3: Magnetic scalar potential ϕ (1st row: imaginary part, 2nd row: real part) and resulting power density μ of heat sources (3rd row) fow three different domain sizes. See text for discussion of results.

the coil rings and in the apparatus) agree up to 3 digits between Ω_{medium} and Ω_{large}. The same holds true for the total heating powers $P_{\text{total}}^{[\text{coil}]}$ and $P_{\text{total}}^{[\text{apparatus}]}$. In consequence Ω_{medium} provides a reasonable compromise between accuracy and computing expenditure and is thus used for all computations of heat sources in Sec. 3.3.

	Ω_{small}	Ω_{medium}	Ω_{large}
$\text{Re}(\phi)_{\text{min}}$ [10^{-6} Wb/m]	-8.74	-8.77	-8.76
$\text{Re}(\phi)_{\text{max}}$ [10^{-6} Wb/m]	4.68	4.61	4.61
$\text{Im}(\phi)_{\text{min}}$ [10^{-4} Wb/m]	-1.66	-1.66	-1.66
$\text{Im}(\phi)_{\text{max}}$ [10^{-4} Wb/m]	0.00	0.00	0.00
$\mu_{\text{max}}^{[\text{coil}]}$ [10^8 W/m^3]	4.83	4.70	4.69
$\mu_{\text{max}}^{[\text{apparatus}]}$ [10^7 W/m^3]	1.49	1.51	1.50
$P_{\text{total}}^{[\text{coil}]}$ [kW]	1.89	1.82	1.82
$P_{\text{total}}^{[\text{apparatus}]}$ [kW]	5.30	5.37	5.37
$P_{\text{total}}^{[\text{coil}]} + P_{\text{total}}^{[\text{apparatus}]}$ [kW]	7.19	7.19	7.19

Table 1: Extreme values of the real and imaginary parts of the magnetic scalar potential, maximal values of power densities, and values of total powers established during numerical simulations on Ω_{small}, Ω_{medium}, and Ω_{large}.

The results depicted in Fig. 3 concur qualitatively with the results found in [PAC+99, Fig. 3] and [CZP+99, Fig. 2].

While a frequency of 10 kHz is not high enough to produce a full-fledged skin effect, the heat sources decay quickly below a conductor's surface (s. Fig. 3(3), where the maximal power density is established in the lower right-hand corner of the graphite).

The values for $P_{\text{total}}^{[\text{coil}]}$ and $P_{\text{total}}^{[\text{apparatus}]}$ in Tab. 1 show that some 25 percent of $P_{\text{total}}^{[\text{coil}]} + P_{\text{total}}^{[\text{apparatus}]}$ is lost in the coil rings.

3.3 Transient Simulation of the Temperature Evolution

In this section we report on transient numerical simulations of the temperature evolution in the growth apparatus, each run starting at $T = 293$ K. We varied the parameters for argon pressure, heating voltage, and vertical coil positions, to assess their influence during the heating process.

It was found in Sec. 3.2 that the domain Ω_{medium} of radius 1.2 m and height 1.8 m is suitable for accurate heat source computations. Hence Ω_{medium} is used for all heat source simulations in the current section. The heat source distribution is computed in each time step of the transient simulations to allow for the temperature dependence of electrical conductivities (cf. Eqs (A.1)). The temperature distribution is only calculated in the growth apparatus, i.e. on a much smaller grid G_T than the grid G_μ used for the heat source computations. In consequence in each time step data for T are carried from G_T to G_μ and data for μ are carried from G_μ to G_T.

In a preparatory set of transient computations we studied the influence of the gas pressure on the temperature distribution, varying argon pressure $p^{(\mathrm{Ar})}$ between 10^{-3} and 10^5 Pa. For these simulations we used $V_{\mathrm{eff}} = 230$ V, and the coil was positioned between $z = 2$ cm and $z = 16$ cm. To allow the prescription of $p^{(\mathrm{Ar})}$, (1.1b) was modified to

$$\frac{3p^{(\mathrm{Ar})}}{2}\frac{\partial \ln T}{\partial t} - \operatorname{div}\left(\kappa^{(\mathrm{Ar})} \operatorname{grad} T\right) = 0, \tag{3.2}$$

which is achieved by inserting (1.2) and the gas law $\rho^{(\mathrm{Ar})} = \frac{M^{(\mathrm{Ar})}p^{(\mathrm{Ar})}}{RT}$ into (1.1b). The temperature distribution was found to be nearly independent of the gas pressure, as e.g. the differences in gas temperatures for $p^{(\mathrm{Ar})} = 10^{-3}$ and $p^{(\mathrm{Ar})} = 10^5$ were $< 10^{-1}$ percent at 300 s, $< 10^{-2}$ percent at 3 000 s, and $< 10^{-6}$ percent at 30 000 s. This result is not surprising, since in the pressure range between 10^{-3} and 10^5 Pa the relaxation time of the temperature in the gas phase always lies orders of magnitude below the corresponding relaxation times in the solid components. Since the gas does not have a significant influence on the temperature of the solid parts, each temporal snapshot of a transient simulation furnishes the quasi-stationary temperature distribution in the gas phase determined by the temperature distribution on the adjacent solid surfaces. If the gas phase is motionless, this quasi-stationary temperature distribution does not depend on the gas pressure.

For the remaining experiments instead of using a given argon pressure, we fixed $\rho^{(\mathrm{Ar})} = 3.73 \cdot 10^{-3}$ kg/m^3, which corresponds to $T = 2575$ K and $p^{(\mathrm{Ar})} = 2 \cdot 10^3$ Pa.

We now discuss four series of numerical experiments referred to as C_0^{14}, C_2^{16}, C_4^{18}, and $\mathrm{C}_{4\to0}^{18\to14}$, each series using a different vertical coil position. For C_0^{14} the coil is positioned between $z = 0$ and $z = 14$ cm, i.e. the lower rim of the bottom coil ring is at $z = 0$ and the upper rim of the top coil ring is at $z = 14$ cm. The meaning of C_2^{16} and C_4^{18} is analogous. For $\mathrm{C}_{4\to0}^{18\to14}$ the coil is moving downwards at the rate 1.33 cm/h between the indicated positions. Here our objective is to study how a moving coil affects the temperature field evolution during the heating process. In this article we do not investigate coil movements that follow the growing crystal in the quasi-stationary temperature field which are often used in growth experiments to compensate the influence of the growing crystal on the temperature distribution. The rate of such coil movements is usually in the order of 1 mm/h. During the simulations $\mathrm{C}_{4\to0}^{18\to14}$ the grid for the heat source computations is newly generated in each time step. There are five experiments in each series using different values for V_{eff}, namely $V_{\mathrm{eff}} = 190$ V, 210 V, 230 V, 250 V, and 270 V. We show results for the time evolution of the total heating power (Fig. 4), for the time evolution (Figs 5 and 6) and the final values (Fig. 7) of T_{top}, T_{bottom}, T_{seed}, and $T_{\mathrm{source}} - T_{\mathrm{seed}}$, for the time evolution of the global temperature field and the heat sources (Fig. 8), and for quasi-stationary temperature distributions at the crystal and its immediate surroundings (Fig. 9). We now proceed to discuss each figure in detail.

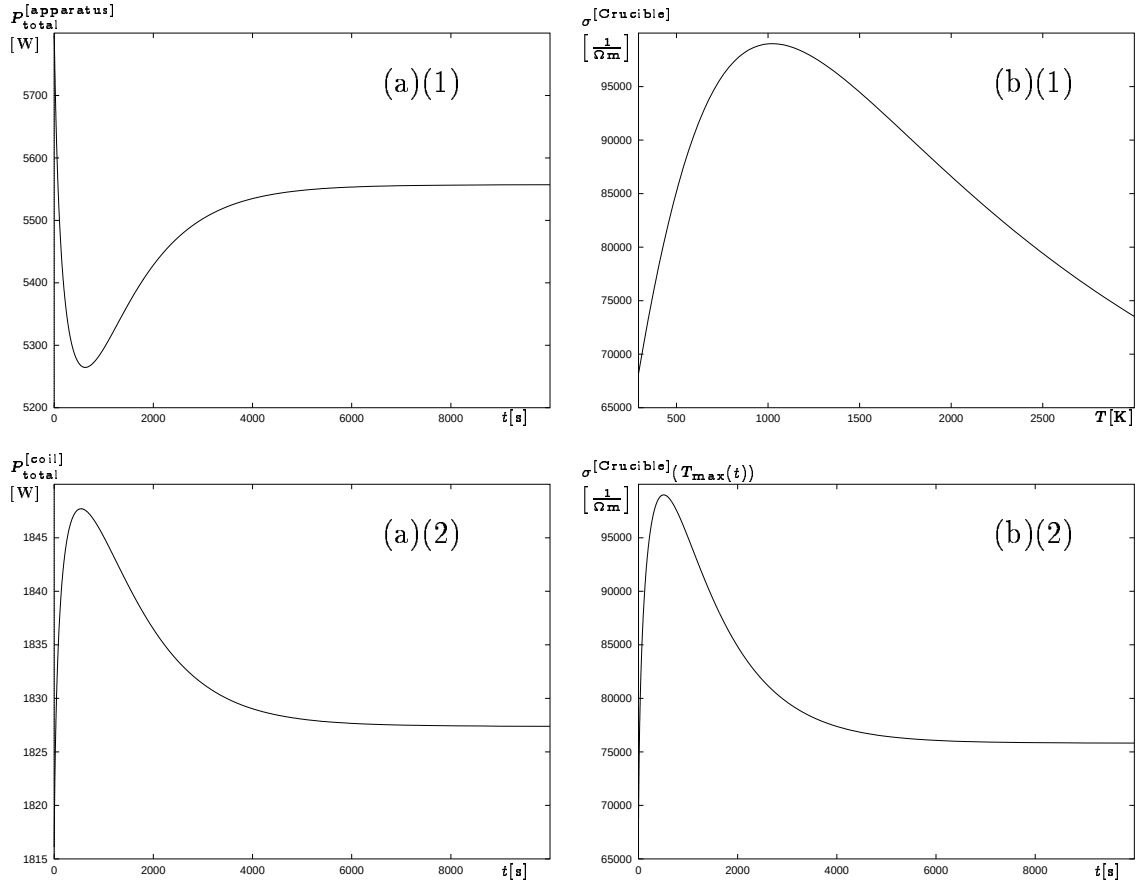

Figure 4: Time evolution of total heating power in growth apparatus (a)(1) and in coil rings (a)(2) for numerical experiment C_2^{16}-230 V in comparison with the temperature-dependent electrical conductivity of the graphite crucible (b). See discussion p. 11.

Figure 4: The total heating power in the growth apparatus $P_{\text{total}}^{[\text{apparatus}]}$ and in the coil rings $P_{\text{total}}^{[\text{coil}]}$ changes during each simulation run due to the temperature-dependent electrical conductivities, and for $C_{4\to 0}^{18\to 14}$ also due to the changing coil positions. Figures 4(a)(1) and (a)(2) depict the time evolution of $P_{\text{total}}^{[\text{apparatus}]}$ and $P_{\text{total}}^{[\text{coil}]}$ for C_2^{16} – 230 V, respectively. The curves show an inverse behaviour, i.e. $P_{\text{total}}^{[\text{apparatus}]}$ decreases as $P_{\text{total}}^{[\text{coil}]}$ increases and vice versa. The peaks after some 500 s in Figs 4(a) correspond to the peaks in Figs 4(b) which show the electrical conductivity of the graphite crucible depending on temperature in (b)(1) and depending on the maximal temperature established in the graphite at time t in (b)(2). The minimum in Fig. 4(a)(1) matches the maximum in Fig. 4(b)(2), showing that the system is in a state where increasing the electrical conductivity of the apparatus (lowering its resistance) reduces $P_{\text{total}}^{[\text{apparatus}]}$. For each simulation Tab. 2 contains $P_{\text{total}}^{[\text{apparatus}]}$ and $P_{\text{total}}^{[\text{coil}]}$ established in the stationary final state.

Figures 5 and 6: Investigation of the temperature evolution at four points of particular importance, located at the blind holes at the top and at the bottom of the growth apparatus, and at the surface of the crystal seed and of the source powder,

V_{eff}[V] / series	190	210	230	250	270	190	210	230	250	270
C_0^{14}	3.46	4.25	5.14	6.11	7.16	1.25	1.53	1.83	2.16	2.51
C_2^{16}	3.74	4.60	5.56	6.60	7.75	1.25	1.53	1.83	2.16	2.51
C_4^{18}	3.90	4.80	5.79	6.88	8.01	1.25	1.52	1.80	2.13	2.48
$C_{4\to0}^{18\to14}$	3.46	4.25	5.14	6.11	7.16	1.25	1.53	1.83	2.16	2.51
	$P_{\text{total}}^{[\text{apparatus}]}$[kW]					$P_{\text{total}}^{[\text{coil}]}$[kW]				

Table 2: Total heating power $P_{\text{total}}^{[\text{apparatus}]}$ in the growth apparatus and $P_{\text{total}}^{[\text{coil}]}$ in the coil rings for the stationary final state, depending on heating voltage and coil positions. respectively (labeled T_{top}, T_{bottom}, T_{seed}, and T_{source} in Fig. 1). The significance of T_{top} and T_{bottom} lies in the blind holes being the principal locations for temperature measurements; T_{seed} and T_{source} are of interest, since their difference is a key control factor for the crystal's growth rate and quality (cf. e.g. [Kon95], [SBP98]). Figures 5 and 6 show the time evolution of T_{top} (row (1)), T_{bottom} (row (2)), T_{seed} (row (3)), and $T_{\text{source}} - T_{\text{seed}}$ (row (4)) for the four simulation series C_0^{14} (Fig. 5, column (a)), C_2^{16} (Fig. 5, column (b)), C_4^{18} (Fig. 6, column (a)), and $C_{4\to0}^{18\to14}$ (Fig. 6, column (b)).

The pictures in rows (1), (2), and (3) show the temperatures increasing from room temperature to growth temperature. For each temporal snapshot the temperatures depend nearly linearly on the heating voltage V_{eff} (for the quasi-stationary state this fact is also illustrated in Fig. 7 below). Moreover, T_{top}, T_{seed}, and T_{source} raise significantly between C_0^{14} (low coil position) and C_4^{18} (high coil position), whereas T_{bottom} remains almost constant. This can be explained by the heat sources being shifted upwards and the source powder's isolating property which, though less prominent, is still effective even at high temperatures (cf. Fig. 8(a) and [KPSW01, (A.6b)]), thereby hindering heat generated below the source powder at reaching regions above the source powder.

The shape of the curves in row (4) of Figs 5 and 6 depicting $T_{\text{source}} - T_{\text{seed}}$ is also due to the isolating characteristic of the source powder and the gas phase, initially keeping the powder's surface below the temperature of the seed which the heat reaches via conduction through the graphite. This causes the negative peak in the corresponding graphs. At higher temperatures radiative heat transfer becomes more effective both in the gas phase and the porous source, resulting in the source growing warmer than the seed, as is required for crystal growth.

In $C_{4\to0}^{18\to14}$ the coil starts out at the position used for C_4^{18} and ends up at the position used for C_0^{14}. As expected, the curves for the moving coil (Fig. 6(b)) initially coincide with the corresponding curves of C_4^{18} (Fig. 6(a)) and coincide with the corresponding curves of C_0^{14} (Fig. 5(a)) after the coil's lowest position is reached at $t = 3$ h.

Figure 7: The values of T_{top} (in (1)), T_{bottom} (in (2)), T_{seed} (in (3)), and $T_{\text{source}} - T_{\text{seed}}$ (in (4)) are considered at the quasi-stationary state in dependence of heating voltage and vertical coil positions. The temperature is seen to depend nearly linearly on the heating voltage. A higher coil position results in T_{top} and T_{seed} being raised significantly, while T_{bottom} remains almost constant, which is due to the changing

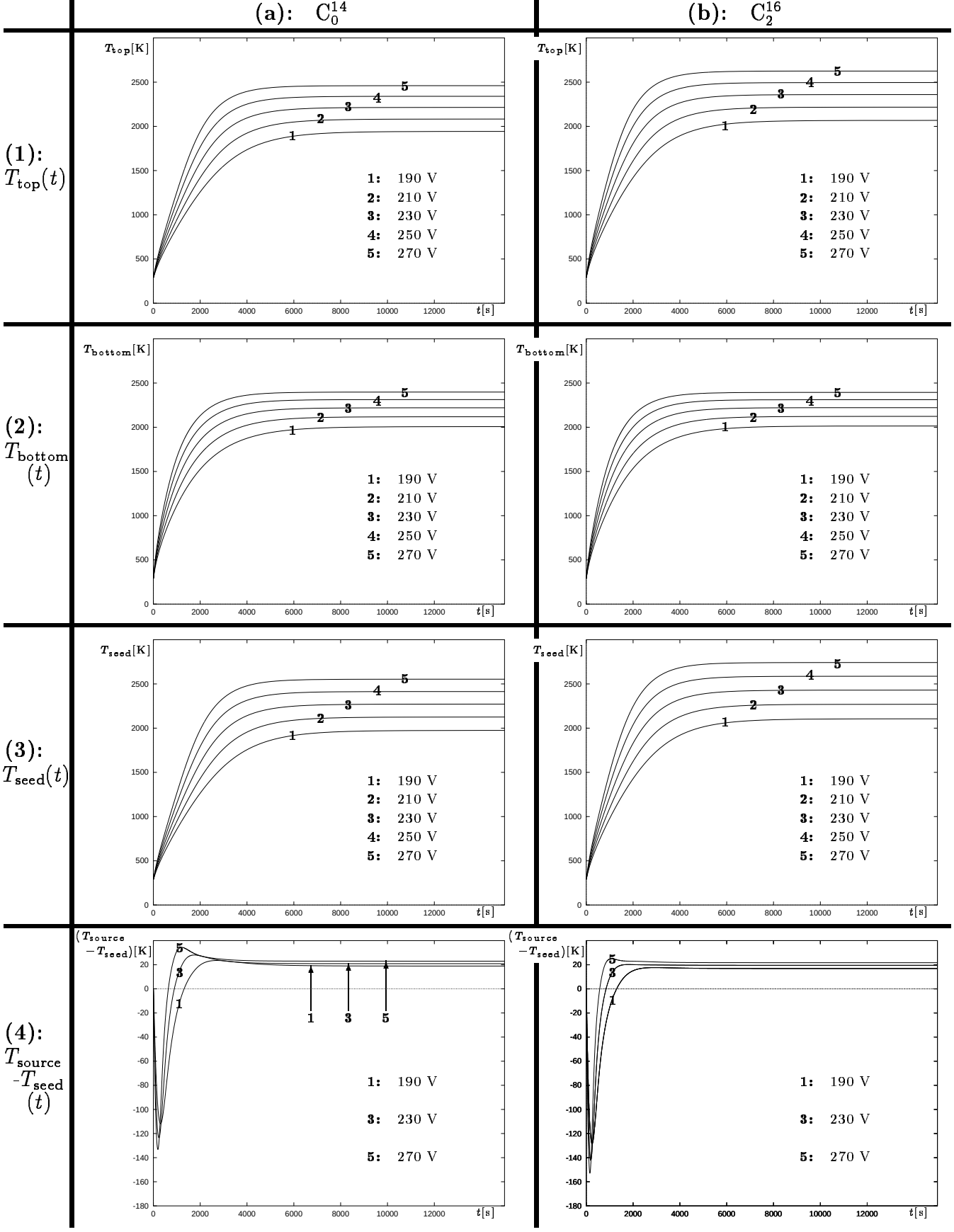

Figure 5: Time evolution of T_{top} (row (1)), T_{bottom} (row (2)), T_{seed} (row (3)), and $T_{\mathrm{source}} - T_{\mathrm{seed}}$ (row (4)) for the simulation series C_0^{14} (column (a)) and C_2^{16} (column (b)). See discussion p. 11 – 12.

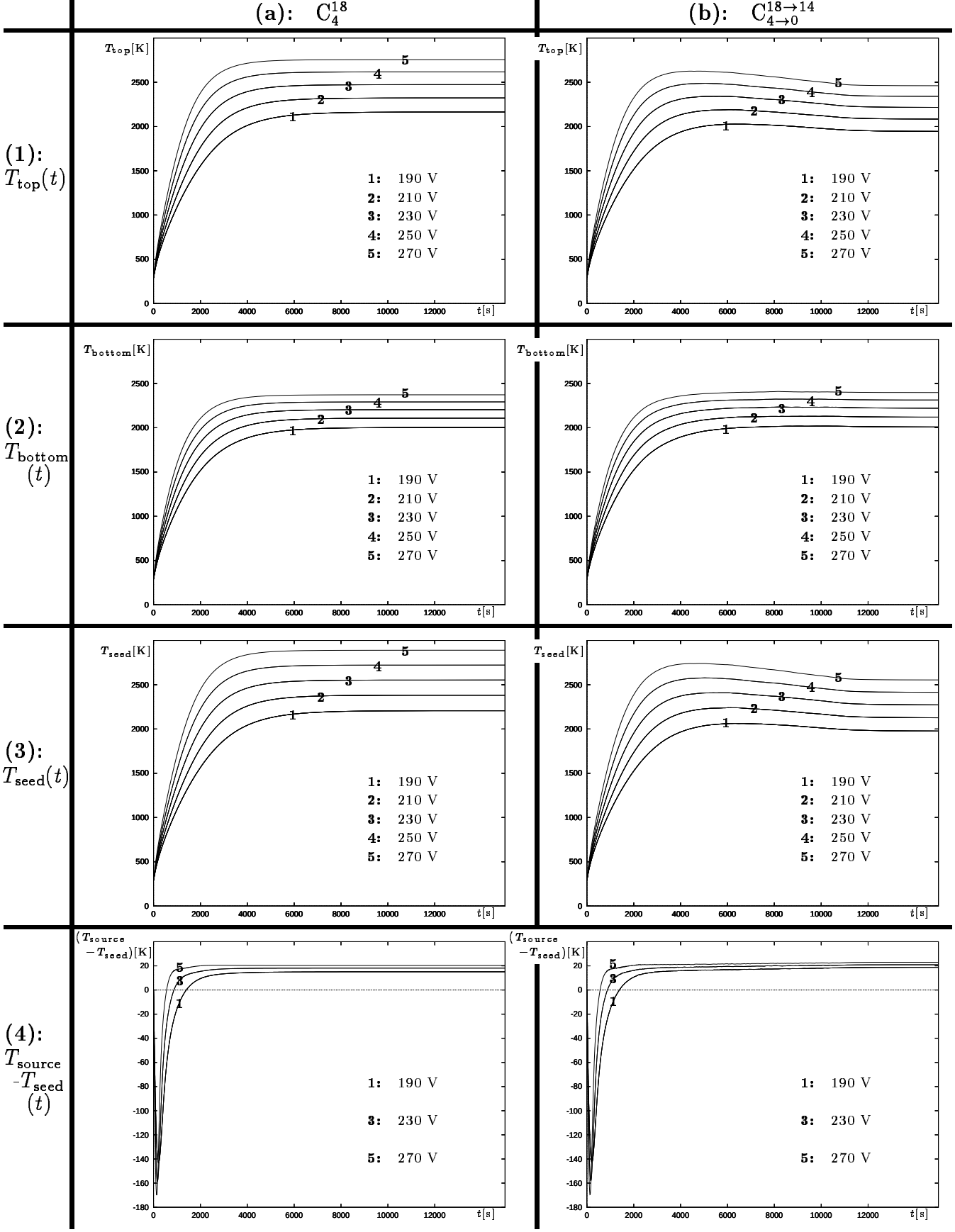

Figure 6: Time evolution of T_{top} (row (1)), T_{bottom} (row (2)), T_{seed} (row (3)), and $T_{\mathrm{source}} - T_{\mathrm{seed}}$ (row (4)) for simulation series C_4^{18} (column (a)) and $C_{4\to0}^{18\to14}$ (column (b)). See discussion p. 11 – 12.

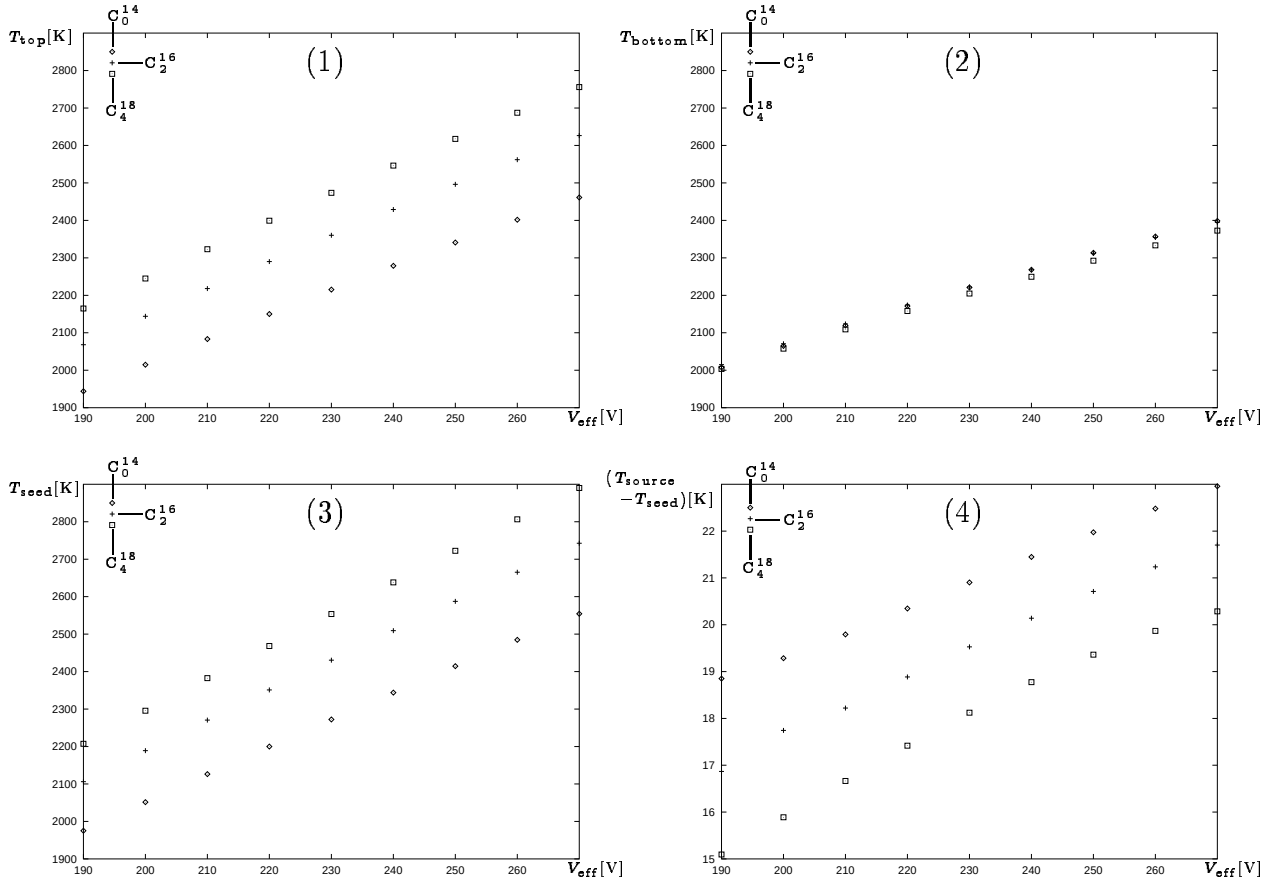

Figure 7: Temperatures T_{top} (in (1)), T_{bottom} (in (2)), T_{seed} (in (3)), and $T_{\mathrm{source}} - T_{\mathrm{seed}}$ (in (4)) for the quasi-stationary state at $t = 30\,000$ s for the simulation series C_0^{14}, C_2^{16}, and C_4^{18} depending on the effective heating voltage. See discussion p. 12 - 15.

heat source distribution and the powder's isolating property as discussed earlier with respect to Figs 5 and 6. Moreover, a higher coil position or a higher heating voltage result in $T_{\mathrm{source}} - T_{\mathrm{seed}}$ being increased as heat reaches the powder's surface more readily at higher temperatures due to radiative heat transfer. Comparing our findings in Fig. 7(4) with [BSG+91, Fig. 6] establishes a qualitative agreement, whereas a quantitative comparison is meaningless due to the different setups. Figure 7(4) indicates that $T_{\mathrm{source}} - T_{\mathrm{seed}}$ can be tuned effectively by controling the heating voltage and the vertical coil position.

Figure 8: Three snapshots of the time evolution of global temperature distribution (column (a), isotherms spaced at 20 K) and heat sources (column (b), isolevels spaced at 0.1 kW/m^3, dark regions indicate larger heat sources) during experiment $C_{4\to0}^{18\to14}$-230 V. The minimal temperature T_{min} is always established at the outside of the outer insulation material, where the isotherms become very dense at higher temperatures, producing the dark outer regions in Fig. 8 (1)(a) and (2)(a). The maximal temperature T_{max} is found in the graphite strip between source and insulation in Fig. 8 (1)(a) and inside the circular-shaped isotherms below the source in Fig. 8 (2)(a) and (3)(a), as the heat sources move downwards together with the induction coil according to Fig. 8(b). Figure 8(a) also illustrates the evolution of

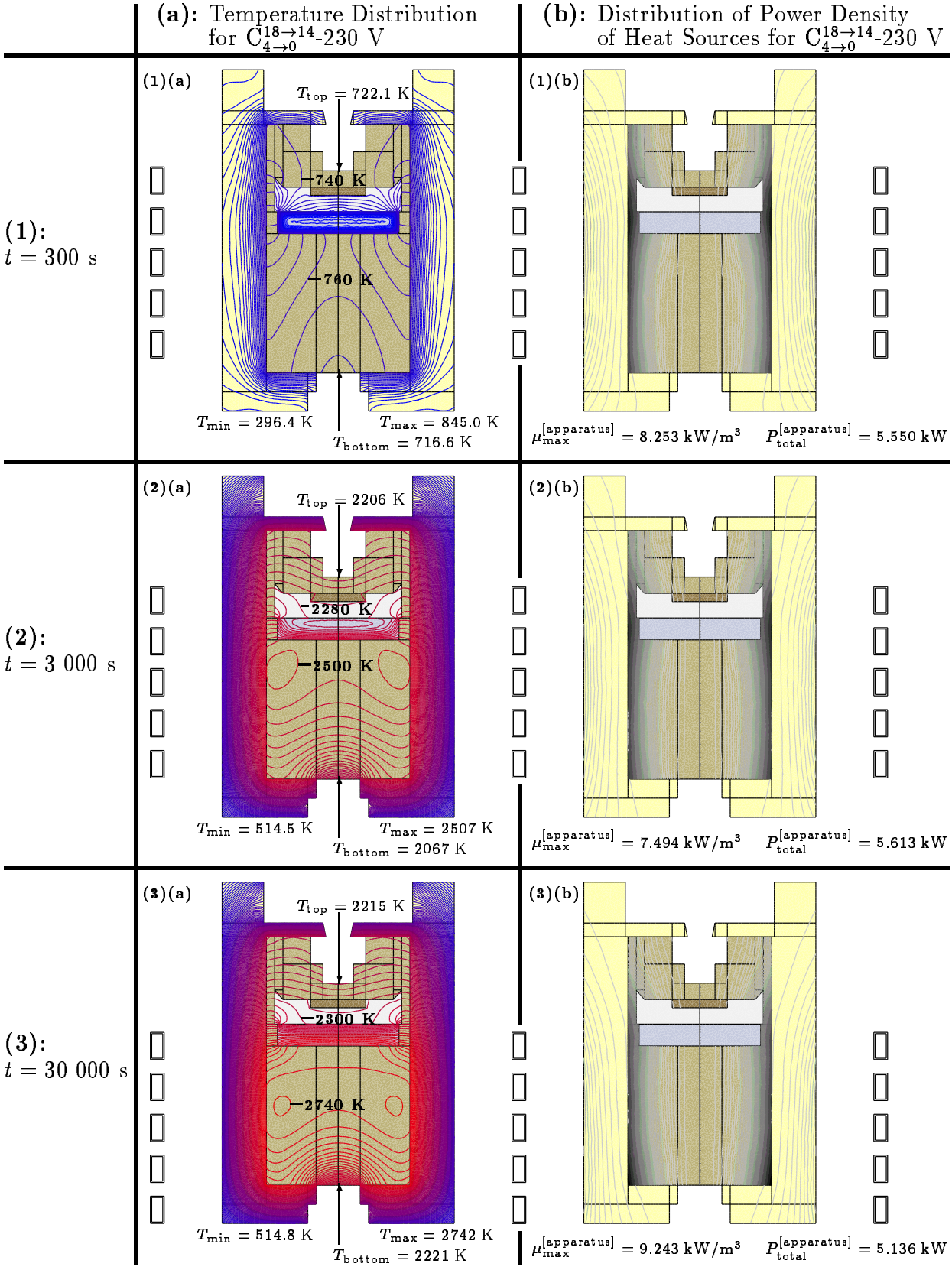

Figure 8: Time evolution of heating process for numerical experiment $C_{4\to0}^{18\to14}$-230 V (coil moving at -1.33 cm/h). Column (a): temperature evolution, difference between neighboring isotherms is 20 K. Column (b): heat source evolution, difference between isolevels is 0.1 kW/m^3, darker regions indicate larger heat sources. See discussion p. 15 – 17.

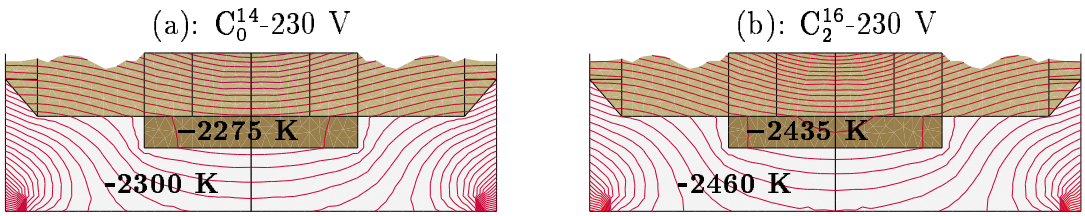

Figure 9: Close-ups of the temperature distribution in the crystal, the gas phase, and the crucible directly above the crystal for the quasi-stationary states at $t = 30\,000$ s of the numerical experiments with lowest and medium coil position in (a) and (b), respectively. Temperature difference between neighboring isotherms is 5 K. See discussion p. 17.

the isolating behaviour of the gas phase and the source, causing a large temperature gradient in the gas phase in 8(1)(a) and local minima in the source in 8(1)(a) and (2)(a). Due to radiative heat transfer through the gas phase and through the pores of the source, the temperature on the boundary of the growth chamber (and hence also inside the gas itself) is more homogeneous in 8(2)(a) and (3)(a), and the local minimum has vanished in Fig. 8(3)(a), even though some of the source's isolating quality persists. The increase in $P_{\mathrm{total}}^{[\mathrm{apparatus}]}$ between Figs 8(1)(b) and (2)(b) followed by the drop between Figs 8(2)(b) and (3)(b) is consistent with Fig. 4(a)(1) and Tab. 2, the increase corresponding to the rise after the initial minimum in Fig. 4(a)(1) and the drop matching the power's decrease with a lower coil position found in Tab. 2.

Figure 9: Close-ups of the final temperature distributions in the crystal's immediate surroundings for two coil positions C_0^{14}-230 V (in (a)) and C_2^{16}-230 V (in (b)), where the picture in (a) also constitutes a close-up of Fig. 8(3)(a), since the stationary states are identical for the simulations C_0^{14}-230 V and $C_{4\to0}^{18\to14}$-230 V. As mentioned during the discussion of Figs 5 and 6, the powder source forms a barrier for heat generated in the lower part of the apparatus. This causes the lower temperatures for the lower coil position found in Fig. 9. Moreover, Fig. 9 shows that the final temperature gradient between source and seed is nearly independent of the coil position and approximately constant along the $r = 0$ axis with a slight increase at the seed.

4 Conclusions

The influence of induction heating during PVT was studied by means of transient numerical simulations including diffusive and radiative heat transfer, where a quasi-stationary elliptic problem is solved in each time step to determine temperature- and coil-position-dependent heat sources. We presented results of computed temperature evolutions depending on heating voltage and vertical coil position. The results agree with physical expectations and provide insights on how to control both the global temperature distribution evolution and the temperature evolution at the seed and the source by adjusting heating voltage and vertical coil position.

Acknowledgements

The IKZ in Berlin has provided us with material data and experimental data throughout the project. In particular we wish to thank Klaus Böttcher, Thomas Müller, Detlev Schulz, and Dietmar Siche. We also thank Jürgen Sprekels and Manfred Uhle of the WIAS in Berlin for helpful discussions and advice.

This research was partly funded by the *Bundesministerium für Bildung, Wissenschaft, Forschung und Technologie*[2] *(BMBF)* within the programs *Neue Mathematische Verfahren in Industrie und Dienstleistungen*[3] # 03SPM3B5 and *Mathematische Verfahren zur Lösung von Problemstellungen in Industrie und Wirtschaft*[4] # 03SP7FV16.

A Appendix: Material Data for Induction Heating

The relevant materials are argon, which is the only material treated as a perfect isolator, copper, graphite crucible, insulation, SiC powder, and SiC crystal.

In each material the reciprocal of the magnetic permeability is assumed to be $\nu = \mu_0^{-1} = \frac{10^7}{4\pi} \cdot \frac{\mathrm{Am}}{\mathrm{Vs}}$.

Mass Densities of Conducting Materials

material	Cu	graphite crucible	insulation	SiC powder	SiC crystal
$\rho[\frac{\mathrm{kg}}{\mathrm{m}^3}]$	8930	1750	170	1700	3140

Table 3: Mass densities of conducting materials.

The values of Table 3 are according to [Ben90] (Cu), [MSS99a] (graphite crucible, insulation), [MSS99b] (SiC powder), and [NMH+97] (SiC crystal).

Electrical Conductivities of Conducting Materials

According to [Ben90] the value for the electrical conductivity of copper at room temperature is $\sigma^{[\mathrm{Cu}]} = (1.7 \cdot 10^{-8}\,\Omega\mathrm{m})^{-1} = 5.9 \cdot 10^7 \frac{1}{\Omega\mathrm{m}}$.

The material parameters used for the electrical conductivities of the remaining con-

[2] German Ministry for Education, Science, Research, and Technology
[3] New Mathematical Methods in Manufacturing- and Service Industry
[4] Mathematical Methods Solving Problems in Industry and Business

ducting materials are

$$\sigma^{[\mathrm{Crucible}]}(T) = \left(28.9 - 18.8 \exp\left(-\left(\frac{\ln\left(\frac{T}{1023\,\mathrm{K}}\right)}{2.37}\right)^2\right)\right)^{-1} \frac{10^6}{\Omega\mathrm{m}}, \tag{A.1a}$$

$$\sigma^{[\mathrm{Insulation}]}(T) = \frac{245.7}{1 + \frac{T}{2500\,\mathrm{K}}} \frac{1}{\Omega\mathrm{m}}, \tag{A.1b}$$

$$\sigma^{[\mathrm{SiC-Powder}]}(T) = 100 \frac{1}{\Omega\mathrm{m}}, \tag{A.1c}$$

$$\sigma^{[\mathrm{SiC-Crystal}]}(T) = 10^5 \frac{1}{\Omega\mathrm{m}}. \tag{A.1d}$$

(A.1a) is according to [Hus84], (A.1b), (A.1c), and (A.1d) are according to [Råb96].

References

[Ben90] G. Benkowsky. *Induktionserwärmung. Härten, Glühen, Schmelzen, Löten, Schweißen*, 5th ed., Verlag Technik GmbH, Berlin, 1990 (German).

[BKP+99] N. Bubner, O. Klein, P. Philip, J. Sprekels, and K. Wilmański. *A transient model for the sublimation growth of silicon carbide single crystals.* J. Crystal Growth **205** (1999), 294–304.

[BMH+93] D.L. Barrett, J.P. McHugh, H.M. Hobgood, R.H. Hopkins, P.G. McMullin, R.C. Clarke, and W.J. Choyke. *Growth of large SiC single crystals.* J. Crystal Growth **128** (1993), 358–362.

[BSG+91] D.L. Barrett, R.G. Seidensticker, W. Gaida, R.H. Hopkins, and W.J. Choyke. *SiC boule growth by sublimation vapor transport.* J. Crystal Growth **109** (1991), 17–23.

[CAB+99] K. Chourou, M. Anikin, J.M. Bluet, J.M. Dedulle, R. Madar, M. Pons, E. Blanquet, C. Bernard, P. Grosse, C. Faure, G. Basset, and Y. Grange. *Modelling of SiC sublimation growth process: analyses of macrodefects formation.* Mater. Sci. Eng. B **61-62** (1999), 82–85.

[col96] *Modelling and optimization of distributed parameter systems (Warsaw, 1995)*, New York, Chapman & Hall, 1996.

[col97] *Modeling and Computation in Environmental Sciences*, Notes on Numerical Fluid Mechanics, vol. 59, Braunschweig, Germany, Vieweg, 1997.

[CZP+99] Q.-S. Chen, H. Zhang, V. Prasad, C.M. Balkas, and N.K. Yushin. *A System Model for Silicon Carbide Crystal Growth by Physical Vapor Transport Method.* 1999 National Heat Transfer Conference, NHTC99-222, ASME, 1999, pp. 1–8.

[FKL98] J. Fuhrmann, Th. Koprucki, and H. Langmach. *pdelib: An open modular tool box for the numerical solution of partial differential equations. Design patterns*, Proceedings of the 14th GAMM Seminar on Concepts of Numerical Software, Kiel, Notes on Numerical Fluid Mechanics, Vieweg, Braunschweig, Germany, 1998, in press.

[Fuh97] J. Fuhrmann. *On numerical solution methods for nonlinear parabolic problems*, in [col97], pp. 170–180.

[Har95] G.L. Harris (ed.). *Properties of Silicon Carbide*, EMIS Datareview Series, no. 13, Institution of Electrical Engineers, INSPEC, London, 1995.

[Hus84] J.G. Hust (ed.). *Standard Reference Materials: Fine-grained, isotropic graphite for use as NBS thermophysical property RM's from 5 to 2500 K*, Tech. Report NBS/SP-260/89, National Bureau of Standards, September 1984.

[KKZ+00] S.Yu. Karpov, A.V. Kulik, I.A. Zhmakin, Yu.N. Makarov, E.N. Mokhov, M.G. Ramm, M.S. Ramm, A.D. Roenkov, and Yu.A. Vodakov. *Analysis of sublimation growth of bulk SiC crystals in tantalum container.* J. Crystal Growth **211** (2000), 347–351.

[KMR97] S.Yu. Karpov, Yu.N. Makarov, and M.G. Ramm. *Simulation of Sublimation Growth of SiC Single crystals.* Phys. Stat. Sol. (b) **202** (1997), 201–220.

[Kon95] A.O. Konstantinov. *Sublimation growth of SiC*, in [Har95], pp. 170–203.

[KPSW01] O. Klein, P. Philip, J. Sprekels, and K. Wilmański. *Radiation- and convection-driven transient heat transfer during sublimation growth of silicon carbide single crystals.* J. Crystal Growth **222** (2001), 832–851.

[MGH+00] St.G. Müller, R.C. Glass, H.M. Hobgood, V.F. Tsvetkov, M. Brady, D. Henshall, J.R. Jenny, D. Malta, and C.H. Carter Jr. *The status of SiC bulk growth from an industial point of view.* J. Crystal Growth **211** (2000), 325–332.

[MSS99a] T. Müller, D. Schulz, and D. Siche. 1999, material vendor's data, communicated by the Institut für Kristallzüchtung, Berlin.

[MSS99b] T. Müller, D. Schulz, and D. Siche. Institut für Kristallzüchtung, Berlin, 1999, unpublished experimental data.

[NMH+97] O. Nilsson, H. Mehling, R. Horn, J. Fricke, R. Hofmann, S.G. Müller, R. Eckstein, and D. Hofmann. *Determination of the thermal diffusivity and conductivity of monocrystalline silicon carbide (300-2300 K).* High Temp. – High Press. **29** (1997), no. 1, 73–80.

[PAC+99] M. Pons, M. Anikin, K. Chourou, J.M. Dedulle, R. Madar, E. Blanquet, A. Pisch, C. Bernard, P. Grosse, C. Faure, G. Basset, and Y. Grange. *State of the art in the modelling of SiC sublimation growth.* Mater. Sci. Eng. B **61-62** (1999), 18–28.

[Råb96] P. Råback. *Modeling of the Sublimation Growth of Silicon Carbide Crystals*, Ph.D. thesis, Helsinki University of Technology, 1996.

[RMD+99] M.S. Ramm, E.N. Mokhov, S.E. Demina, M.G. Ramm, A.D. Roenkov, Yu.A. Vodakov, A.S. Segal, A.N. Vorob'ev, S.Yu. Karpov, A.V. Kulik, and Yu.N. Makarov. *Optimization of sublimation growth of SiC bulk crystals using modeling.* Mater. Sci. Eng. B **61-62** (1999), 107–112.

[RS96] J. Rappaz and M. Swierkosz. *Modelling in numerical simulation of electromagnetic heating*, in [col96], pp. 313–320.

[RSD+99] H.-J. Rost, D. Siche, J. Dolle, W. Eiserbeck, T. Müller, D. Schulz, G. Wagner, and J. Wollweber. *Influence of different growth parameters and related conditions on 6H-SiC crystals grown by the modified Lely method.* Mater. Sci. Eng. B **61-62** (1999), 68–72.

[SBP98] N. Schulze, D.L. Barrett, and G. Pensl. *Near-equilibrium growth of mircopipe-free 6H-SiC single crystals by physical vapor transport.* Appl. Phys. Lett. **72** (1998), no. 13, 1632–1634.

[SKM+00] M. Selder, L. Kadinski, Yu. Makarov, F. Durst, P. Wellmann, T. Straubinger, D. Hoffmann, S. Karpov, and M. Ramm. *Global numerical simulation of heat and mass transfer for SiC bulk crystal growth by PVT.* J. Crystal Growth **211** (2000), 333–338.

[SVK+00] A.S. Segal, A.N. Vorob'ev, S.Yu. Karpov, E.N. Mokhov, M.G. Ramm, M.S. Ramm, A.D. Roenkov, Yu.A. Vodakov, and Yu.N. Makarov. *Growth of silicon carbide by sublimation sandwich method in the atmosphere of inert gas.* J. Crystal Growth **208** (2000), 431–441.